OPEN EUROPEAN JOURNAL ON VARIABLE STARS
http://oejv.physics.muni.cz
July 2023 DOI: 10.5817/OEJV2023-0237 ISSN 1801–5964

PROPERTIES OF THE LOW-AMPLITUDE W URSAE MAJORIS BINARY GSC 02873-03309

Christopher Lloyd, Ian Miller *

Department of Physics and Astronomy, University of Sussex, Brighton, BN1 9QH C.Lloyd@sussex.ac.uk

Abstract: GSC 02873-03309 is a low-amplitude W Ursae Majoris eclipsing binary with a period of 0.4996319(2) d. The eclipses have depths of 0.107 and 0.102 mag in the TESS data suggesting a low inclination. The absolute magnitude is consistent with other W UMa systems of similar period, and there is currently no evidence of period change.

GSC 02873-03309 (UCAC4 671-018057, 03 20 11.866 +44 10 37.80 *Gaia* DR3) was identified as a low-amplitude W Ursae Majoris variable by Miller (2016) while making time-series observations of the UGSW variable SDSS J032015.29+441059.3. The star has $V \sim 13.9$ with an amplitude of 0.1 mag, and a period very close to half a day. The observations were made at the Furzehill Observatory using a 0.35m SCT and SXVR-H16 CCD camera over six nights during October 2016 and a further run in January 2018, as listed in Table 1. The images were processed using the *API4WIN* aperture photometry package relative to an ensemble of comparison stars from the AAVSO sequence X16680AAS. The star is also given as the 139 comparison in the archived version of the same sequence. All but the last two runs were unfiltered but calibrated as V to give CV magnitudes, while the last two used a V filter. All the data are available from the BAA VSS Photometry Database and the AAVSO data archive. The early observations were taken over just 14 days and due to the inconvenient period, the phase diagram is incomplete. Although most of the light-curve is covered the primary minimum is not, and none of the individual runs completely cover the secondary eclipse. The final run was taken specifically to capture the primary eclipse and the timing was measured using the Kwee-van Woerden method (Kwee & van Woerden, 1956) so as to obtain a timing completely independent of the other data that were taken some 15 months earlier. The formal error has been increased by a factor of 1.5 to account for the likely underestimation of this method (see Mikulášek et al., 2014). The secondary timing was measured from a 4-harmonic Fourier fit to all the data at a fixed period, and the timing of the primary minimum was consistent within the errors with the KvW measurement. More generally here the Fourier fit is used to determine the times of minima as the function is more flexible than say a template or some other pre-determined light-curve profile, so timings are less susceptible to changes in the light-curve, like spots, outside eclipse. The uncertainties on the times of minima from the Fourier fits are determined through a method of redistributed residuals. The phase diagram of the time-series data is shown in Figure 1.

The star has since been reported as variable in data from the All-Sky Automated Survey for Supernovae (ASAS-SN) project (Shappee et al., 2014; Kochanek et al., 2017), the Asteroid Terrestrial-Impact Last Alert System (ATLAS) project (Tonry et al., 2018;

*Ian Miller (1946 – 2020) https://furzehillobservato.wixsite.com/furzehillobservatory/about-me

July 2023 DOI: 10.5817/OEJV2023-0237 ISSN 1801–5964

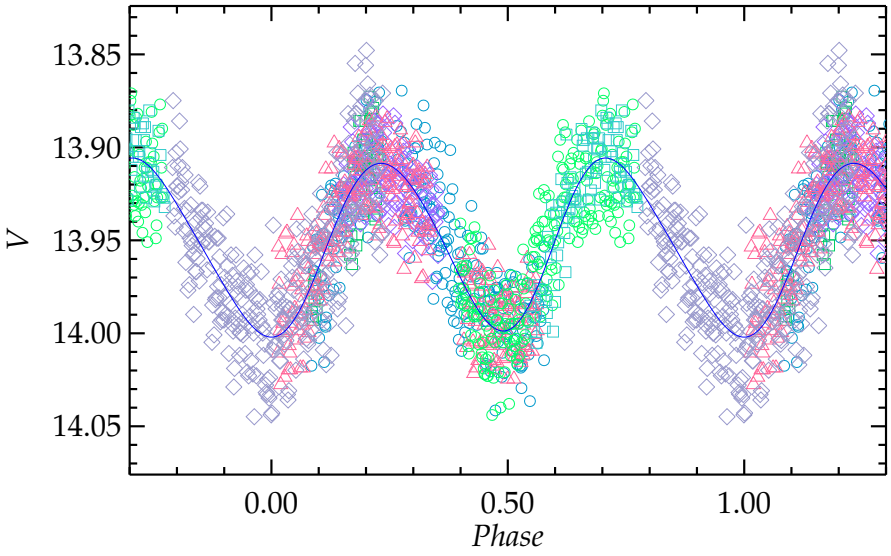

Figure 1: The phase diagram of the time-series data folded on the best fit period given in Equation 2. Different runs are shown with different symbols.

Smith et al., 2020) and the Zwicky Transient Facility (ZTF) (Masci et al., 2019) although Chen et al. (2020) find an alias of the correct period. The other potentially useful data set comes from the Northern Variability Sky Survey (NSVS)(Woźniak et al., 2004) and pre-dates the time-series data by 16 years, but unfortunately they are noisy and heavily flagged, and do not generate a usable phase diagram.

All the ground-based observations struggle to provide reliable light curves because the star is relatively faint, the amplitude is low, and the period is close to half a day. Consequently, the seasonal phase diagrams are often poorly covered so in order to make reliable eclipse timings it is necessary to use data covering two or more years. ASAS-SN observations are typically made in groups of three in the space of 0.003 d or 4 minutes, and measurements have been taken from the direct aperture photometry pipeline of the individual images. Composite timings have been derived using 2-harmonic Fourier fits to data from 2014–2018 in V and 2018–2023 in Sloan g. The full ASAS-SN phase diagrams are given in Figure 2.

Table 1: Observing log of the time-series runs

Date	JD	Hours	Band	N
2016 Oct 01	2457663.392 - .638	5.9	CV	263
2016 Oct 03	2457665.391 - .461	1.7	CV	46
2016 Oct 04	2457666.420 - .524	2.5	CV	126
2016 Oct 05	2457667.354 - .628	6.6	CV	299
2016 Oct 11	2457672.542 - .728	4.5	CV	234
2016 Oct 14	2457675.615 - .728	2.7	V	81
2018 Jan 06	2458125.401 - .623	5.3	V	287

 DOI: 10.5817/OEJV2023-0237 ISSN 1801–5964

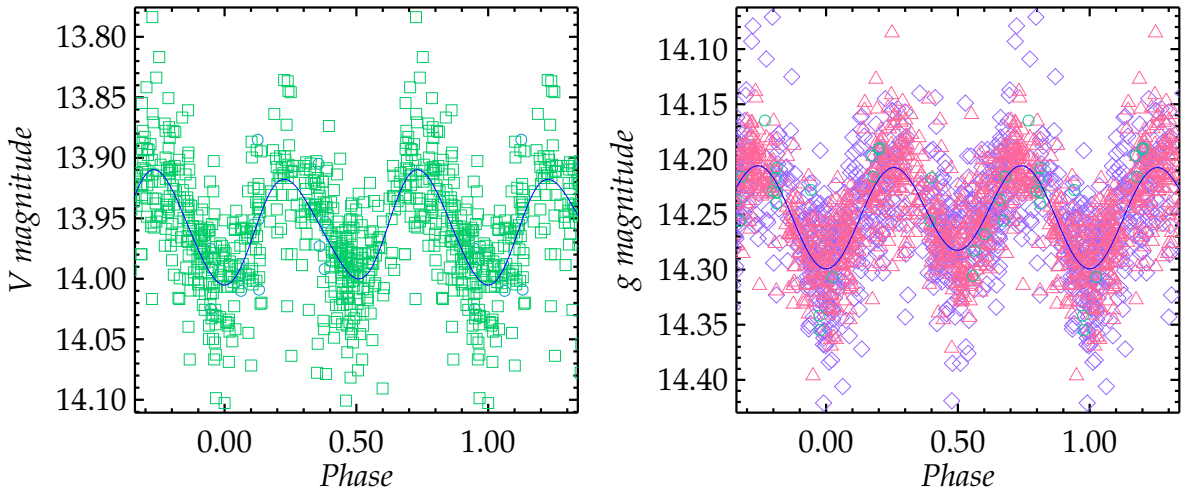

Figure 2: The phase diagrams of the ASAS-SN V- (left) and g-band data (right) folded on the best fit period given in Equation 2. Different cameras are shown with different symbols. Figures 3 and 4 are plotted at the same scale.

Data from the ATLAS project are typically made in groups of four over about an hour in the cyan and orange bands, so come from one cycle. Observations were downloaded from the ATLAS Forced Photometry Server using the simple aperture photometry option and multi-year composite timings derived as above for 2016–2023, using both the cyan and the rather more reliable orange-band data. The cyan data are much more sparse so not all the sets provided times of both primary and secondary minima. The full ATLAS phase diagrams are given in Figure 3. Data from the ZTF project are available as individual

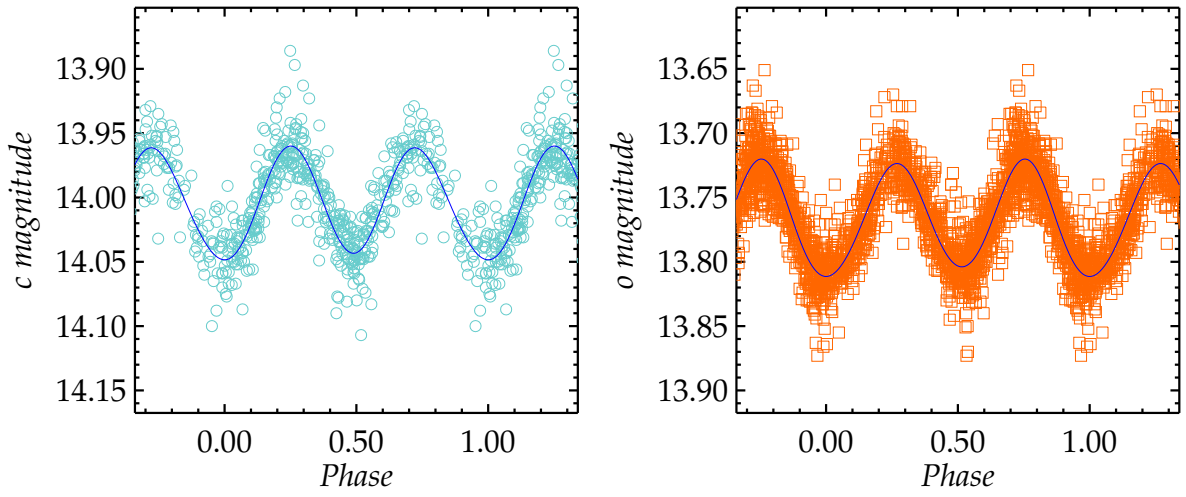

Figure 3: The phase diagrams of the ATLAS cyan- (left) and orange-band data (right) folded on the best fit period given in Equation 2. The diagram is plotted at the same scale as Figure 2.

July 2023 DOI: 10.5817/OEJV2023-0237 ISSN 1801–5964

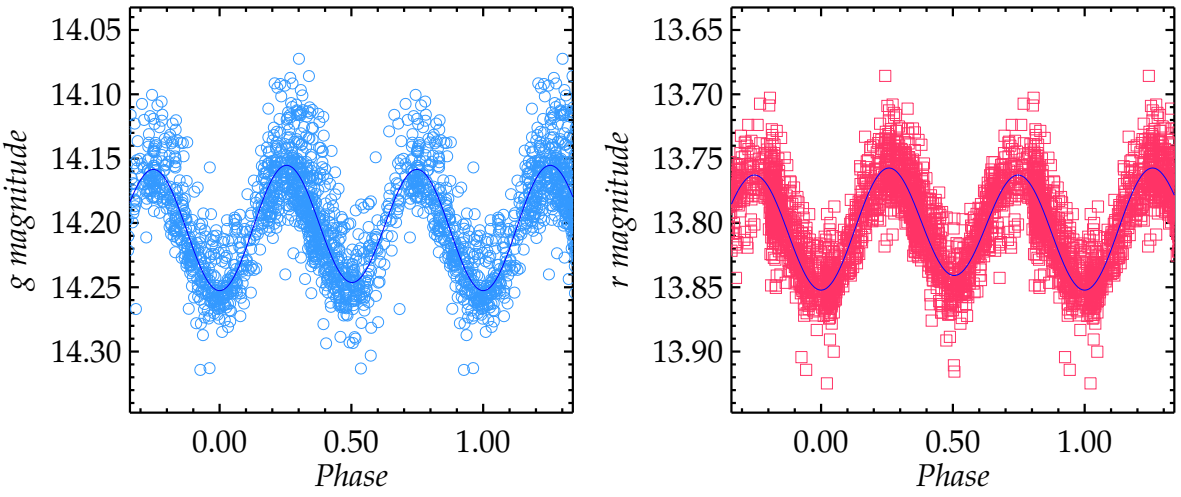

Figure 4: The phase diagrams of the ZTF g- (left) and r-band data (right) folded on the best fit period given in Equation 2. The diagram is plotted at the same scale as Figure 2.

observations from 2018–2023, in the g and r bands. Although there are approximately 1200 and 1900 observations respectively, the unhelpful period means that multi-season composite timings are still necessary. Heliocentric corrections have been applied to the original (M)JD or UTC dates as appropriate using the Terrestrial Time (TT) date and are within a few seconds of BJD.

The rms residuals from the Fourier fits are 0.020 mag for the time-series data, 0.02–0.03 mag for ATLAS and ZTF, and 0.03–0.04 mag for the ASAS-SN data. For the synoptic data sets the residuals were limited to 4σ, which excluded the most discordant data, but this was not necessary for the time-series observations. For reasons that are not clear the synoptic photometry seems to have a long tail of excessive residuals, which combined with the half-day period hinders accurate eclipse timings. Despite the shallow minima and the relatively large residuals the primary minimum is correctly identified in all the data sets, and in all but the ASAS-SN data the maximum at phase 0.25 is the slightly brighter one. The amplitude from the Fourier fits is very similar in all bands with $\Delta V = 0.09$ mag in both the time-series and ASAS-SN data, $\Delta g = 0.10$ mag, $\Delta r = 0.10$ mag, and the ATLAS $\Delta o = \Delta c = 0.09$ mag. The temperature difference between components in W UMa systems is generally small, < 1000 K, and there is no indication of any significant difference from the variation in different bands.

GSC 02873-03309 has also been observed by the Transiting Exoplanet Survey Satellite (TESS) (Ricker et al., 2015) during November 2019 in Sector 18 at the standard 30-minute cadence, and during November 2022 in Sector 58 with a much higher cadence of 200 seconds. The data were extracted from the Full-Frame Images using the *Lightkurve* package (Lightkurve Collaboration et al., 2018) and restricted to HARD quality in *Lightkurve* parlance. The fluxes were measured using the default aperture created within the routine but due to the faintness of the target, the high background and the contamination by a nearby star, the default aperture was limited to one and two pixels in the two sectors.

July 2023 DOI: 10.5817/OEJV2023-0237 ISSN 1801–5964

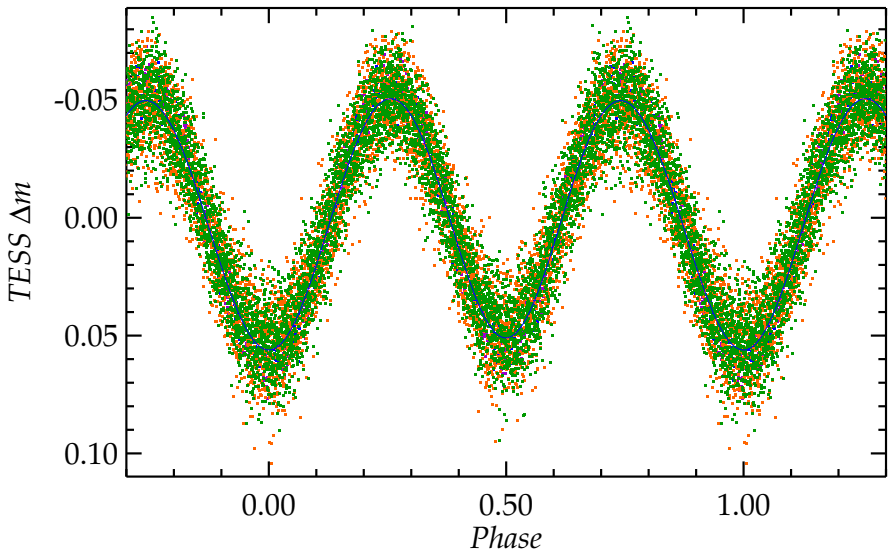

Figure 5: The phase diagram of the TESS data folded on the best fit period given in Equation 2. The different half-sectors are shown in different colours.

However, the light-curve is still diluted by the background and restricted to an amplitude of 0.04 mag, which is less than half that seen in the ground-based photometry. The sky background was measured in a one-pixel wide frame, one pixel removed from the default aperture, and this was subtracted from the target flux. The sky-subtracted flux shows the full amplitude of the light-curve and is also better corrected in the high-noise sections of data. The resulting light-curve is relatively smooth but some discordant sections were removed and additional flattening with a low-order polynomial fitting was required to correct variation in level through the TESS orbit, as is often the case. The sky-subtracted flux allows much more of the raw data to be used, but this comes at the cost of higher noise levels in some sections of the data. The TESS sectors naturally divide into two due to the 1–2 day break for the data downlink so the light-curve comprises four sections of $\sim$ 11 days of mostly continuous data. The phase diagram is shown in Figure 5 with a 4-harmonic Fourier fit. There is no systematic deviation from the mean light-curve and the residuals have an rms error of 0.012 mag. The amplitudes of primary and secondary eclipses are 0.107 and 0.102 mag – marginally larger than the ground-based data – and the maxima are the same to 0.001 mag. Timings for both minima (strictly BJD) were measured for each of the half-sectors and these are collected with all the other times of minimum in Table 2.

The problems with phase coverage of the ground-based observations means that despite the multi-year data sets some of the minima are not sufficiently well covered and coupled with the low amplitude of the variation, the uncertainties on the eclipse timings are relatively large. Nevertheless, only the most doubtful and those with the largest errors have been excluded to give the most complete picture of the period behaviour possible. The ephemeris has been calculated from a weighted fit to subsets of the minima, using the formal errors on the timings where $w_i = 1/\sigma_i^2$. The weighted fits to all the data

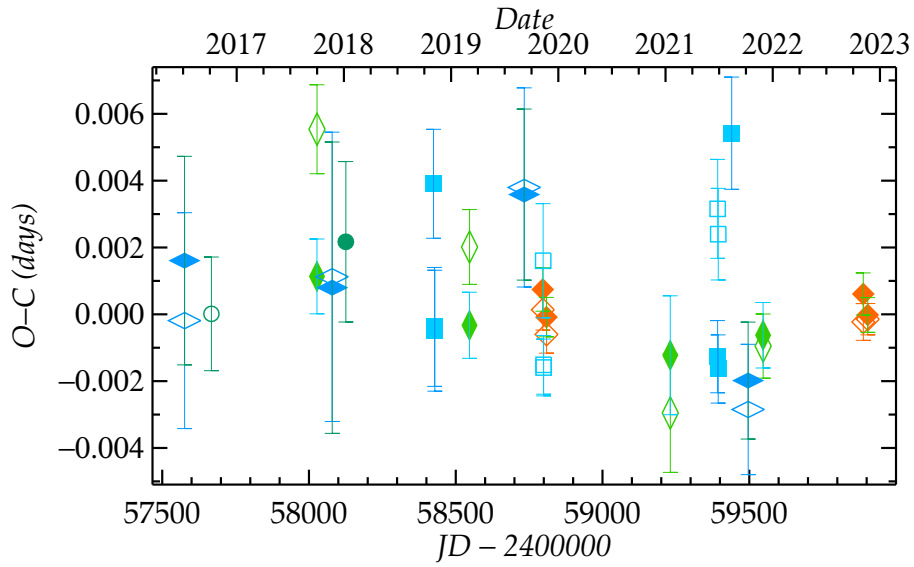

Figure 6: O-C diagram of the times of minima from Table 2 showing the time-series points (circles), the ASAS-SN V and g-band data (flat lozenges), the ATLAS data (tall lozenges), the ZTF data (squares), and the TESS data (diamonds). Open symbols show the secondary minima. The diagram is constructed using the ephemeris derived from the TESS minima in Equation 2.

and the non-TESS subset give reduced chi-squared, $\chi^2_\nu = 2.00$, and 2.26 respectively, suggesting that either the errors are underestimated, or that there is additional variation in the timings due to changes in the shape of the light-curve. To derive the most reliable estimate of the uncertainty on the ephemeris the errors have been scaled to give $\chi^2_\nu = 1$. The ephemeris from all the data is

$$HJD_{\mathrm{MinI}} = 2458796.50672(27) + 0.49963166(19) \times E \quad (1)$$

but due to their much smaller errors this solution is still influenced by the TESS data, which on their own give

$$HJD_{\mathrm{MinI}} = 2458796.50647(30) + 0.49963190(18) \times E \quad (2)$$

which has $\chi^2_\nu = 0.62$, suggesting that if anything, the TESS errors might be overestimated. The non-TESS data on their own give an acceptably consistent ephemeris

$$HJD_{\mathrm{MinI}} = 2458796.50674(40) + 0.49963121(35) \times E \quad (3)$$

However, given the much higher quality and consistency of the TESS data, that solution is preferred, and there is no evidence of any period change.

The period of GSC 02873-03309 lies at the break point of the empirical Period-Luminosity relationship between the early- and late-type W UMa systems (see e.g., Jayasinghe et al., 2020), and broadly corresponds to the transition region between rapidly and slowly rotating main-sequence stars, referred to as the Kraft break (Kraft, 1967). The discrimination between the two groups occurs over the temperature range $T_{\mathrm{eff}} =$

July 2023 DOI: 10.5817/OEJV2023-0237 ISSN 1801–5964

Table 2: Times of minima

HJD	Error	Min.	Cycle	O-C	Band	Source
2457575.9074	0.0031	1	−2443.0	0.0016	*V*	ASAS-SN
2457576.1554	0.0032	2	−2442.5	−0.0002	*V*	ASAS-SN
2457667.5882	0.0017	2	−2259.5	0.0000	*CV*	Miller
2458027.0745	0.0011	1	−1540.0	0.0011	*o*	ATLAS
2458027.3287	0.0013	2	−1539.5	0.0055	*o*	ATLAS
2458078.7864	0.0043	2	−1436.5	0.0011	*V*	ASAS-SN
2458079.0359	0.0044	1	−1436.0	0.0008	*V*	ASAS-SN
2458125.5030	0.0024	1	−1343.0	0.0022	*V*	Miller
2458424.2846	0.0016	1	−745.0	0.0039	*g*	ZTF
2458427.7778	0.0018	1	−738.0	−0.0004	*r*	ZTF
2458428.7769	0.0018	1	−736.0	−0.0005	*r*	ZTF
2458546.6902	0.0010	1	−500.0	−0.0003	*o*	ATLAS
2458546.9423	0.0011	2	−499.5	0.0020	*o*	ATLAS
2458733.0568	0.0026	1	−127.0	0.0036	*g*	ASAS-SN
2458733.3068	0.0030	2	−126.5	0.0038	*g*	ASAS-SN
2458796.5072	0.0007	1	0.0	0.0007	*C*	TESS
2458796.7564	0.0006	2	0.5	0.0001	*C*	TESS
2458797.7571	0.0017	2	2.5	0.0016	*g*	ZTF
2458799.2528	0.0009	2	5.5	−0.0016	*r*	ZTF
2458799.2529	0.0009	2	5.5	−0.0015	*r*	ZTF
2458808.9972	0.0006	1	25.0	−0.0001	*C*	TESS
2458809.2465	0.0006	2	25.5	−0.0006	*C*	TESS
2459230.6854	0.0018	1	869.0	−0.0012	*c*	ATLAS
2459230.9334	0.0018	2	869.5	−0.0030	*c*	ATLAS
2459392.0664	0.0011	1	1192.0	−0.0013	*r*	ZTF
2459392.3207	0.0015	2	1192.5	0.0032	*r*	ZTF
2459394.0646	0.0010	1	1196.0	−0.0016	*r*	ZTF
2459394.3184	0.0014	2	1196.5	0.0024	*r*	ZTF
2459440.0378	0.0017	1	1288.0	0.0054	*g*	ZTF
2459495.9891	0.0018	1	1400.0	−0.0020	*g*	ASAS-SN
2459496.2381	0.0019	2	1400.5	−0.0028	*g*	ASAS-SN
2459546.9529	0.0010	1	1502.0	−0.0006	*o*	ATLAS
2459547.2024	0.0010	2	1502.5	−0.0010	*o*	ATLAS
2459888.2028	0.0006	1	2185.0	0.0006	*C*	TESS
2459888.4518	0.0005	2	2185.5	−0.0002	*C*	TESS
2459903.6907	0.0005	1	2216.0	0.0000	*C*	TESS
2459903.9404	0.0005	2	2216.5	−0.0001	*C*	TESS

$6200 - 6700$ K so Jayasinghe et al. also provide a luminosity calibration in the $T_{\rm eff}$-Period plane. All the luminosity relationships for both period and $T_{\rm eff}$ ranges suggest that the absolute magnitude of the system is $M_{\rm V} \approx 2.4$ and $M_{\rm g} \approx 2.4$ mag. More general relationships based on a smaller sample of stars by Mateo & Rucinski (2017) suggest $M_{\rm V} \sim 2.8$ mag. At the distance $d = 1480 \pm 35$ pc from Bailer-Jones et al. (2021) the red-

dening is $E(g-r) = 0.13 \pm 0.02$ mag (Green et al., 2019) or $E(B-V) = 0.20 \pm 0.03$ mag (Lallement et al., 2018), which with $E(B-V) \approx E(g-r)$ at small values, $R_{\rm V} = 3.1$, and $V = 13.95$ mag, leads to $M_{\rm V} = 2.4 - 2.7$ mag, and this is broadly consistent with the value based on the period. Using the *Gaia* distance and reddening, and the BP/RP spectra assuming a single star, the Apsis processing chain Creevey et al. (2022) finds $M_{\rm g} = 2.78$ mag, which is 0.4 mag fainter than the value based on the period. However, the Apsis distance is 150 pc closer than that of Bailer-Jones et al. which could account for an ~ 0.2 mag reduction in luminosity.

Jayasinghe et al. (2020) provide temperature calibrations for the early and late populations which at $P = 0.5$ d give $T_{\rm eff} = 7041$ and 6596 K respectively. Temperatures estimated from the relationships of Latković et al. (2021) and Poro et al. (2022) also suggest $T_{\rm eff} \sim 6900$ K. The *Gaia* DR3 Apsis processing based on the reddening and the BP/RP spectra gives $T_{\rm eff} = 6492$ K and this is more consistent with the cool-star calibration. Different LAMOST spectral calibrations also give $T_{\rm eff} \sim 6600$ K (see e.g., Xiang et al., 2019).

The main point of contention is the cause of the shallow eclipses, and in many cases this is due to dilution through the presence of a luminous third body. In this case there is no evidence of a third body in the distribution of the residuals in the O–C diagram, although the time scale is rather short, but the best evidence comes from the absolute magnitude, which is certainly no brighter than that expected for a system of this period. It therefore appears most likely that the system simply has a low inclination. The other point to emerge is that the system probably belongs to the cool population despite its relatively long period.

Acknowledgements: The authors appreciate the assistance of Klaus Bernhard. The authors are pleased to acknowledge use of NASA's Astrophysics Data System Bibliographic Services. This research has made use of the SIMBAD database and the VizieR catalogue access tool, CDS, Strasbourg, France (DOI: 10.26093/cds/vizier). This paper includes data collected by the TESS mission, which are publicly available from the Mikulski Archive for Space Telescopes (MAST). Funding for the TESS mission is provided by NASA's Science Mission directorate.

References

Bailer-Jones, C. A. L., Rybizki, J., Fouesneau, M., et al., 2021, *AJ*, **161**, 147, 2021AJ....161..147B

Chen, X., Wang, S., Deng, L., et al., 2020, *ApJS*, **249**, 18, 2020ApJS..249...18C

Creevey, O. L., Sordo, R., Pailler, F., et al., 2022, *arXiv e-prints*, arXiv:2206.05864, 2022arXiv220605864C

Green, G. M., Schlafly, E., Zucker, C., et al., 2019, *ApJ*, **887**, 93, 2019ApJ...887...93G

Jayasinghe, T., Stanek, K. Z., Kochanek, C. S., et al., 2020, *MNRAS*, **493**, 4045, 2020MNRAS.493.4045J

Kochanek, C. S., Shappee, B. J., Stanek, K. Z., et al., 2017, *PASP*, **129**, 104502, 2017PASP..129j4502K

Kraft, R. P., 1967, *ApJ*, **150**, 551, 1967ApJ...150..551K

Kwee, K. K. & van Woerden, H., 1956, *Bulletin of the Astronomical Institutes of the Netherlands*, **12**, 327, 1956BAN....12..327K

Lallement, R., Capitanio, L., Ruiz-Dern, L., et al., 2018, *A&A*, **616**, A132, 2018A&A...616A.132L

Latković, O., Čeki, A., & Lazarević, S., 2021, *ApJS*, **254**, 10, 2021ApJS..254...10L

Lightkurve Collaboration, Cardoso, J. V. d. M., Hedges, C., et al., 2018, , Astrophysics Source Code Library, record ascl:1812.013, 2018ascl.soft12013L

Masci, F. J., Laher, R. R., Rusholme, B., et al., 2019, *PASP*, **131**, 018003, 2019PASP..131a8003M

Mateo, N. M. & Rucinski, S. M., 2017, *AJ*, **154**, 125, 2017AJ....154..125M

Mikulášek, Z., Chrastina, M., Liška, J., et al., 2014, *Contributions of the Astronomical Observatory Skalnate Pleso*, **43**, 382, 2014CoSka..43..382M

Miller, I., 2016, *British Astronomical Association Variable Star Section Circular*, **170**, 8, 2016BAAVC.170....8M

Poro, A., Sarabi, S., Zamanpour, S., et al., 2022, *MNRAS*, **510**, 5315, 2022MNRAS.510.5315P

Ricker, G. R., Winn, J. N., Vanderspek, R., et al., 2015, *Journal of Astronomical Telescopes, Instruments, and Systems*, **1**, 014003, 2015JATIS...1a4003R

Shappee, B. J., Prieto, J. L., Grupe, D., et al., 2014, *ApJ*, **788**, 48, 2014ApJ...788...48S

Smith, K. W., Smartt, S. J., Young, D. R., et al., 2020, *PASP*, **132**, 085002, 2020PASP..132h5002S

Tonry, J. L., Denneau, L., Heinze, A. N., et al., 2018, *PASP*, **130**, 064505, 2018PASP..130f4505T

Woźniak, P. R., Vestrand, W. T., Akerlof, C. W., et al., 2004, *AJ*, **127**, 2436, 2004AJ....127.2436W

Xiang, M., Ting, Y.-S., Rix, H.-W., et al., 2019, *ApJS*, **245**, 34, 2019ApJS..245...34X